arXiv:1602.00806v1 [astro-ph.HE] 2 Feb 2016

X-ray Spectral Model of Reprocessing by Smooth and Clumpy Molecular Tori in Active Galactic Nuclei with the MONACO framework

Shun'ya Furui[1], Yasushi Fukazawa[1,2,3], Hirokazu Odaka[4,5], Toshihiro Kawaguchi[6], Masanori Ohno[1,3], Kazuma Hayashi[1]

fukazawa@hep01.hepl.hiroshima-u.ac.jp

ABSTRACT

We construct an X-ray spectral model of reprocessing by a torus in an active galactic nucleus (AGN) with a Monte Carlo simulation framework MONACO. Two torus geometries of smooth and clumpy cases are considered and compared. In order to reproduce a Compton shoulder accurately, MONACO includes not only free electron scattering but also bound electron scattering. Raman and Reyleigh scattering are also treated, and scattering cross sections dependent on chemical states of hydrogen and helium are included. Doppler broadening by turbulence velocity can be implemented. Our model gives consistent results with other available models, such as MYTorus, except for differences due to different physical parameters and assumptions. We studied the dependence on torus parameters for Compton shoulder, and found that a intensity ratio of Compton shoulder to line core mainly depends on the column density, inclination angle, and metal abundance. For instance, an increase of metal abundance makes the Compton shoulder relatively weak. Also, shape of Compton shoulder depends on the column density. Furthermore, these dependences become different between smooth and clumpy cases. Then, we discuss the possibility of *ASTRO-H* SXS spectroscopy of Compton shoulder in AGN reflection spectra.

Subject headings: galaxies: active — X-rays: galaxies

[1]Department of Physical Science, Hiroshima University, 1-3-1 Kagamiyama, Higashi-Hiroshima, Hiroshima 739-8526, Japan

[2]Hiroshima Astrophysical Science Center, Hiroshima University, 1-3-1 Kagamiyama, Higashi-Hiroshima, Hiroshima 739-8526, Japan

[3]Core Research for Energetic Universe (Core-U), Hiroshima University, 1-3-1 Kagamiyama, Higashi-Hiroshima, Hiroshima 739-8526, Japan

[4]Kavli Institute for Particle Astrophysics and Cosmology, Stanford University 2575 Sand Hill Rd, Menlo Park, CA 94025

[5]Institute of Space and Astronautical Science (ISAS), Japan Aerospace Exploration Agency (JAXA), 3-1-1 Yoshinodai, Chuo, Sagamihara, Kanagawa, 252-5210, Japan

[6]Department of Liberal Arts and Sciences, Sapporo Medical University, S1W17, Chuo-ku, Sapporo 060-8556, Japan

1. Introduction

Active galactic nuclei (AGNs) have supermassive black holes (SMBHs) at the center of each galaxy, and accretion discs surrounding the SMBHs emit an enormous energy of 10^{42}–10^{47} erg s^{-1} from region whose size is as small as the solar system. Based on various observational results, a huge gas-dust structure, so-called "torus", presumably exists around the accretion disc (Antonucci & Miller 1985), and hides the central engine with a substantial fraction from distant observers. The torus is likely composed of inflowing materials from a parent galaxy to an accretion disc and thus related to the evolution of SMBH. For X-ray radiation of AGN, we observe not only a direct (e.g., transmitted) component from accretion disc/corona but also a reprocessed component by the torus. The reprocessed component contains information on such as X-ray fluorescence, absorption and reflection (e.g. Awaki et al. 1991; Fukazawa et al. 2011). Therefore, it is important to clarify what can be learned about the state of matter (e.g., temperature, degree of ionization, and velocity dispersion) via the observed X-ray spectra.

In order to estimate the state of materials in the tori, various X-ray spectral models have been constructed and made comparison with the observed data. Among them, a commonly used model is `pexrav` (Magdziarz & Zdziarski 1995) in XSPEC. This is the reflection model from a flat infinite disc, but fluorescence lines are not included in this model. There is an improved model (`pexmon`) (Nandra et al. 2007) by adding fluorescence lines to the `pexrav` model. Furthermore, more complicated models are available (Ikeda et al. 2009; Murphy & Yaqoob 2009; Brightman & Nandra 2011), and Liu & Li (2014, 2015) has begun to study X-ray spectra from the AGN torus with Geant4, a widely used Monte Carlo simulation library in fields ranging from high-energy particle physics to space science (Ivanchenko et al. 2003). As seen in these models, more realistic shapes of the torus and physical processes have come to be thought in late years, and they enable us to estimate the state of materials in detail. Brightman et al. (2015) reported some comparisons of models of reprocessing by torus among `pexrav`, `MYTorus` (Murphy & Yaqoob 2009), and the model of Brightman & Nandra (2011). However, most of these models fall under any of the following: the distribution of material is smooth, only simple geometry is discussed, and the effect of velocity dispersion and/or scattering with bound electron are not considered.

To sustain the geometrical thickness of the torus, the velocity dispersion must be as large as a typical rotation velocity of the torus, ~ 100 km s^{-1}. However, thermal velocity of these dusty gas cannot become fast up to this speed, because dust grains reach the sublimation temperature $T \sim 1500$ K (Barvainis 1987; Laor & Draine 1993). Therefore, the torus is most likely a group of many dusty clumps with a large velocity dispersion (clumpy torus), rather than a smooth mixture of gas and dust (smooth torus) (Krolik & Begelman 1988). Although simple geometries (e.g., smooth gas fulfilled in doughnuts) have been applied in most torus models for X-ray studies, an actual torus is likely (1) clumpy, and (2) has a concave shape at the innermost region because of anisotropic emissions from the accretion disc (Kawaguchi & Mori 2010; 2011). Moreover, (3) the velocity dispersion of the innermost part is as high as thousands km s^{-1} (Kawaguchi 2013), which inevitably affects the interpretations and predictions for future high-resolution spectroscopy, which

will be realized by the *ASTRO-H* X-ray observatory, scheduled for launch in 2016 (Takahashi et al. 2014).

All these realistic geometrical configurations and kinematics should be considered for the analysis of high-resolution spectra. In order to build such a realistic spectral model, we must solve a problem of radiative transfer which requires treatment of a discrete process of a photon, competing processes, and multiple interactions in a complicated geometry. This is obviously difficult by analytical methods, and we therefore adopt a Monte Carlo approach as the `MYTorus` project (Murphy & Yaqoob 2009). As the first step of this project, this paper focuses on the effects of the clumpiness and the velocity dispersion, though we still use a simple geometry of the entire torus which is adopted in `MYTorus`. Our simulation model is constructed with a Monte Carlo simulation framework, `MONACO` (MONte Carlo simulation for Astrophysics and COsmology), which was originally developed and verified in the context of X-ray reflection nebulae in the Galactic Center region (Odaka et al. 2011).

In the Compton-thick reflection case, a conspicuous feature, so-called Compton shoulder, is formed in adjacent to emission lines, after scattering of line photons. Since the shape of Compton shoulder changes with various parameters such as the state of scattering electron (free or bound, etc.) and the kinematics of materials, the Compton shoulder is a strong probe to investigate the state of matter around the black hole (Murphy & Yaqoob 2009). Matt (2002) presented the dependence of the Compton shoulder against the column density and inclination angle, but only for reflector geometry of sphere or plane. Yaqoob and Murphy (2011) studied the Compton shoulder for the reflector geometry of smooth torus, and mainly showed the dependence of the Compton shoulder shape on the column density, inclination, incident spectral slope, and velocity dispersion. Our simulator based on `MOCACO` includes accurate physical processes considering Compton scattering by not only free electrons but also bound electrons in atoms or molecules for hydrogen and helium. Since these processes are not included properly in other works, we are able to investigate the shape of Compton shoulder more accurately and in detail. In addition, we for the first time study the Compton shoulder for the clumpy torus.

In this work, we present results of simulations on a smooth and a clumpy torus and discuss the effects of clumpiness. We explain the torus geometry, the Monte Carlo code, and the simulation process in Section 2. We present results of the reflection continuum and Compton shoulder in Section 3, followed by discussions in Section 4.

2. Models and Calculation Methods

2.1. Torus Geometry and Material Properties

We construct both smooth and clumpy torus models for the Monte Carlo simulations. Figure 1 shows the cross-section view of these tori: the smooth one is shown in the left panel and the

clumpy one in the right. In the both models, matter is distributed in a common torus geometry that is determined by the opening angle $\theta_{\rm OA}$ and the major radius $R_{\rm torus}$ of the torus surrounding the central black hole. The smooth torus has a uniform hydrogen number density $n_{\rm H}$ and therefore the column density measured along a line on the equatorial plane from the central black hole is given by $N_{\rm H} = 2n_{\rm H}R_{\rm torus}\cos\theta_{\rm OA}$. We assume chemical composition of solar values obtained by Anders & Grevesse (1989), and elemental abundances of metals (lithium and heavier elements) can be scaled by a common factor $A_{\rm metal}$ (metal abundance relative to the solar values). In addition, the simulation is able to treat Doppler effects due to random motion of the torus material. The gas motion is treated as micro-turbulence for simplisity, so the gas velocity has a Gaussian distribution with a standard deviation of $v_{\rm turb}$, which is called a turbulent velocity.

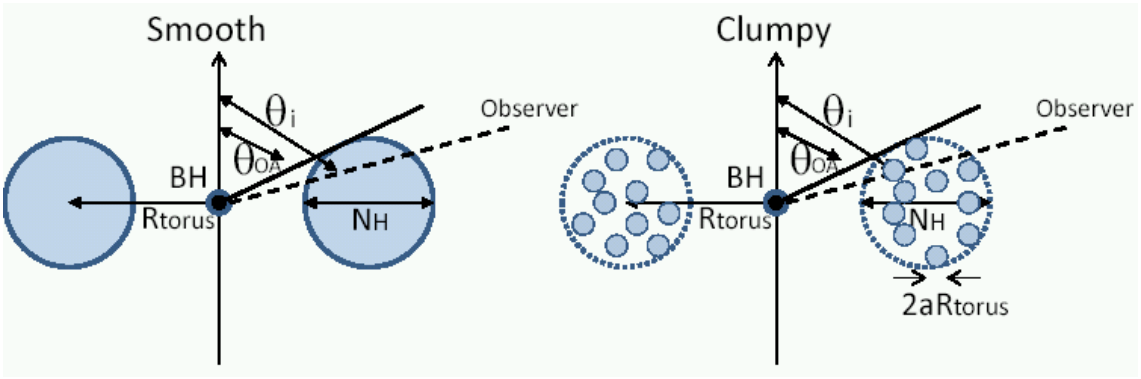

Fig. 1.— Torus geometry implemented in our model for smooth (left) and clumpy (right) cases. Inclination angle θ_i, opening angle $\theta_{\rm OA}$, torus radius $R_{\rm torus}$, column density $N_{\rm H}$ are also shown.

The clumpy torus consists of a number of small spherical clumps all of which have common radius, density, and chemical composition. These clumps are randomly distributed in the torus geometry identical to one adopted in the smooth torus model. The positions of the clumps are randomly determined so as to keep uniformity of the torus. Then, if there are geometrical overlaps between the clumps, the conflicting clumps are rearranged in order to define clumps as geometrically separate objects. We introduce a clump scaling factor a which determines the clump radius as $R_{\rm clump} = aR_{\rm torus}$. The degree of clumpiness is characterized by a volume filling factor f, which is defined as a fraction of volume that is filled with the clumps in the whole torus volume. The number of clumps is calculated to be $fV_{\rm torus}/V_{\rm clump} = (3/2)f\pi a^{-3}\cos^2\theta_{\rm OA}$, where we use that the torus volume is $V_{\rm torus} = 2\pi^2 {R_{\rm torus}}^3\cos^2\theta_{\rm OA}$ and the clump volume is $V_{\rm clump} = (4/3)\pi {R_{\rm clump}}^3$. The hydrogen number density $n_{\rm H}$ in a single clump should be enhanced by a factor of f^{-1} from the number density averaged over the whole torus, namely we have a relation: $N_{\rm H} = 2fn_{\rm H}R_{\rm torus}\cos\theta_{\rm OA}$.

The average number of clumps along a radial equatorial direction is calculated by the product of the clump density in a unit volume $[f/(4\pi R_{\rm clump}^3/3)]$, the cross section of one clump $(\pi R_{\rm clump}^2)$ and the length of the region where clumps are located $(2R_{\rm torus}\cos\theta_{\rm OA})$ (e.g., Kawaguchi & Mori 2011, equation A6). With our fidicial parameters, it is $7.5(f/0.05)(a/0.005)^{-1}(\cos\theta_{\rm OA}/0.5)$, within

the probable range of this quantity (5–15) estimated by Nenkova et al. (2008).

Hydrogen can exist in a state of atom or molecule. Although both forms can be treated as the same way for most of the photon interactions, only Rayleigh scattering for molecular hydrogen should be enhanced by a factor of two per electron because of coherent effects (Sunyaev & Churazov, 1996). Our simulation code is able to treat both atomic hydrogen and molecular hydrogen. Most hydrogens within each clump likely form molecules (e.g., Pier & Voit 1995). For instance, the temperature inside a clump even at the innermost edge of the torus is around 500 K or less (Hönig et al. 2006, their Figure 4 and Table 1). Although hard X-ray photons can reach deep into each clump, a large fraction ($33 - 95\%$) of hydrogen within a clump form molecules (Krolik & Lepp 1989, their Table 2). In this paper, we assume that all hydrogens exist as H_2 molecules.

In short, our model is specified by the geometry of the torus and the material properties (i.e. the chemical composition and the turbulent velocity). Essentially, the column density controls the total amount of the matter; thus, we do not need to care the absolute size of the system. In Table 1, we summarize independent model parameters of the smooth torus model as well as additional parameters of the clumpy torus model.

Table 1: Independent Model Parameters

Common parameters	Range
Torus opening angle $\theta_{\rm OA}$	60°
Column density $N_{\rm H}$	1×10^{21}–1×10^{26} cm^{-2}
Metal abundance $A_{\rm metal}$	0.1–10 solar
Turbulent velocity $v_{\rm turb}$	0–3000 km s^{-1}
Additional parameters of clumpy torus	**Range**
Clump scaling factor a	0.002–0.005
Volume filling factor f	0.01–0.05

2.2. Monte Carlo Code and Photon Interactions

A Monte Carlo approach is suitable for solving radiative transfer in the AGN torus since multiple interactions must be treated in a complicated optically thick geometry. For our simulations, we use `MONACO` (Odaka et al. 2011), a Monte-Carlo calculation framework of X-ray radiation for general astrophysical problems. This code utilizes the Geant4 toolkit library (Agostinelli et al. 2003; Allison et al. 2006) for tracking photons in a complicated geometry. Although Geant4 already has its own physical process libraries mainly for radiation measurements, we do not use them but introduce our original physics implementations required for astrophysical purposes. Several photon processes playing important roles in astrophysics—e.g. photoelectric absorption, scattering, photoionization,

photoexcitation, and Comptonization—are included in MONACO and we select necessary processes among them for the purpose of the simulation. MONACO is able to treat a variety of geometries composed of neutral matter as well as ionized plasma. The Doppler shift and broadening due to bulk and random (thermal and turbulent) motions are also calculated in the photon tracking calculation.

Physics implementation used in this work was originally developed and was verified in the context of X-ray reflection from molecular clouds by Odaka et al. (2011). As described in Section 2.1, we assume that matter in the torus is cold and hydrogens are all in molecular forms. In this condition, we need to consider photoelectric absorption followed by a fluorescence emission and scattering by an electron that is bound to hydrogen and helium as the interactions of photons with matter. MONACO uses the Evaluated Photon Data Library 97 (EPDL97)[1], which is distributed together with the Geant4 library, as cross section data of photoelectric absorption. In our physics implementation, a K-shell fluorescent photon is generated with a probability of a fluorescence yield just after the photoelectric absorption. Atomic properties relevant to the fluorescence, namely K-shell line energies, fluorescence yields, and Kβ-to-Kα ratios are taken from Thompson et al. (2001), Krause et al. (1979), and Ertuğral et al. (2007), respectively. Kα_2-to-Kα_1 intensity ratios are fixed to 0.5. When an Auger electron is generated, tracking is stopped. Table 2 summarizes the energies of K-edge, K-lines, and the fluorescence yields used in our model.

Scattering by electrons also plays an important role in generating spectral features particularly at the hard X-ray band above 10 keV and the Compton shoulders of the iron K line at 6.4 keV. Since most electrons are bound to atoms or molecules in the condition of interest, photons are mostly scattered by electrons bound to hydrogen and helium. Binding an electron to an atom or molecule alters the scattering process, though many previous studies of the AGN reflection had considered only Compton scattering by free electrons at rest. The scattering process by a bound electron can be classified under three channels by difference in the final state of the target electron: (1) Rayleigh scattering to the ground state, (2) Raman scattering to excited states, and (3) Compton scattering to free states (Sunyaev & Churazov, 1996). The shape of the Compton shoulder is greatly modified by the electron binding since the target electron is not at rest but has finite momentum in the atomic or molecular system. Thus, accurate treatment of the scattering process by a bound electron is of great importance in evaluating detailed spectral features measured by high-resolution spectroscopy. Details about the physics implementation are described in Odaka et al. (2011) (see appendix in this reference).

[1]https://www-nds.iaea.org/epdl97/

Table 2: Energies of K-edge, K-lines, and fluorescence yields

Z^a	Element	K-edge^b	Kα_1^b	Kα_2^b	Kβ^b	$Y^c_{K\alpha}$	$Y^c_{K\beta}$
1	H	13.6					
2	He	23.4					
3	Li	59.9	54.30				
4	Be	118.4	108.50				
5	B	195.6	183.30			0.0017	
6	C	291.0	277.00			0.0028	
7	N	404.9	392.40			0.0052	
8	O	537.3	524.90			0.0083	
9	F	688.4	676.80			0.0130	
10	Ne	858.2	848.60	848.60		0.0180	
11	Na	1064.0	1040.98	1040.98	1071.10	0.0230	
12	Mg	1294.5	1253.60	1253.60	1302.20	0.0296	0.0004
13	Al	1549.9	1486.70	1486.27	1557.45	0.0382	0.0008
14	Si	1828.5	1739.98	1739.38	1835.94	0.0487	0.0013
15	P	2130.4	2013.70	2012.70	2139.10	0.0604	0.0026
16	S	2455.9	2307.84	2306.64	2464.04	0.0736	0.0044
17	Cl	2804.9	2622.39	2620.78	2815.60	0.0906	0.0063
18	Ar	3177.6	2957.70	2955.63	3190.50	0.1068	0.0112
19	K	3583.3	3313.80	3311.10	3589.60	0.1258	0.0142
20	Ca	4015.0	3691.68	3688.09	4012.70	0.1452	0.0178
21	Sc	4465.8	4090.60	4086.10	4460.50	0.1668	0.0212
22	Ti	4940.6	4510.84	4504.86	4931.81	0.1897	0.0243
23	V	5439.6	4952.20	4944.64	5427.29	0.2151	0.0278
24	Cr	5957.6	5414.72	5405.51	5946.71	0.2424	0.0325
25	Mn	6510.9	5898.75	5887.65	6490.45	0.2692	0.0388
26	Fe	7083.4	6403.84	6390.84	7057.98	0.3003	0.0398
27	Co	7680.7	6930.32	6915.30	7649.43	0.3275	0.0455
28	Ni	8302.8	7478.15	7460.89	8264.66	0.3583	0.0477
29	Cu	8943.2	8047.78	8027.83	8905.29	0.3873	0.0526
30	Zn	9622.4	8638.86	8615.78	9572.00	0.4166	0.0574

a: atomic number

b: energies in unit of eV

c: fluorescence yield of K lines

2.3. Comparison with the MYTorus model

To demonstrate the performance of our simulation model generated by MONACO, we make a comparison with a widely used X-ray spectral model for AGN torus studies that is also based on Monte Carlo simulations. We select MYTorus (Murphy & Yaqoob, 2009) as a benchmark model since it assumes a simple, well-defined torus geometry with an opening angle of 60° and a metal abundance of 1 solar value, where the solar values are based on Anders & Grevesse (1989). Then, we performed Monte Carlo simulations with MONACO to generate a spectral model for parameters of $\theta_{\rm OA} = 60°$, $A_{\rm metal} = 1.0$, and $N_{\rm H} = 1 \times 10^{24}$ cm^{-2}. The initial spectrum is assumed to be a power law with a photon index of 1.9 in an energy range of 2–300 keV, and 6.4×10^8 incident photons were simulated in total to make the spectrum.

The spectrum emerging from the AGN torus system can be divided into two components, namely direct component and reprocessed component. The direct component is composed of photons that are initially emitted at the central source and then escape from the system without any interaction. The reprocessed component is a result of scattering and fluorescence following photoelectric absorption. Since MONACO is able to distinguish these two components for each observed photon and MYTorus also provides the two components separately, we make the comparison between the two models for each component to demonstrate effects of detailed implementations of the physical processes.

In Figure 2, we show spectra of the direct component for comparison between MONACO and MYTorus. These spectra are extracted by integrating escaping photons that have direction within $0.1 \leq \cos\theta_i < 0.2$ (or $81.4° \pm 2.9$). In this work, we assume that in the AGN torus all electrons responsible for scattering are bound to atoms or molecules, while MYTorus uses Compton scattering by free electrons at rest. In order to check consistency with MYTorus, we compare three spectra: MYTorus model spectrum (red line in the figure), a MONACO spectrum assuming free electrons at rest (green), and a MONACO spectrum assuming electrons bound to hydrogen molecules and helium atoms (blue). The comparison shows excellent agreement among the three models above 10 keV within 5%. In the low energy band, our model of the bound electron case gives a less direct component, and this can be understood as described below for a similar comparison of the scattering component. Also, another difference can be seen in the enlarged view around the iron K-shell edge at 7 keV. The difference in energy of the iron edge comes from difference in the origin of the cross section data of photoelectric absorption used in the two models. The MONACO spectrum of the bound electron scattering shows slightly lower than that of the free electron scattering since a cross section of Rayleigh scattering is enhanced by a factor of two for a hydrogen molecule, resulting in insignificant reduction of the direct component. Note that this direct component is easily calculated by the total cross section (absorption and scattering), which means that we do not need detailed Monte Carlo simulations in practice. MYTorus actually provides the direct component model without Monte Carlo simulations. Here we have verified the Monte Carlo simulations in MONACO by using the direct component which is easily calculated.

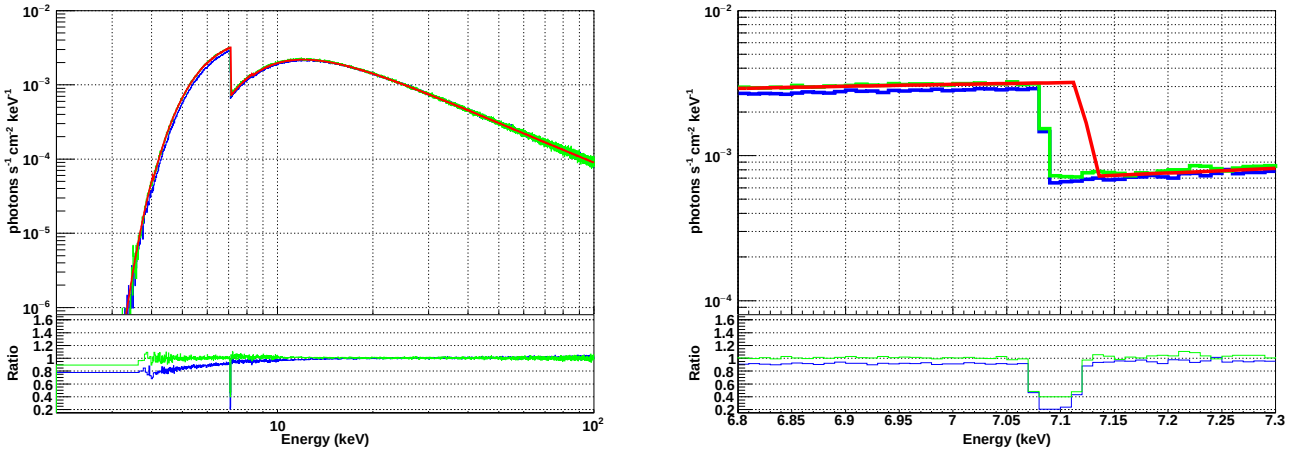

Fig. 2.— Spectra of the direct component for comparison between `MONACO` and `MYTorus`. The left panel is shown in 2–100 keV while the right panel is enlarged around the iron K-shell edge at 7 keV. Three models are shown: the `MYTorus` model (red), the free electron case generated with `MONACO` (green), and the bound electron case generated with `MONACO` (blue). (See text in detail). The bottom panels in each figure are spectral ratios against `MYTorus`.

Then, we compare the reprocessed component, which is best calculated by accurate Monte Carlo simulations. Figure 3 shows the spectra of the reprocessed component given by the three different models. These spectra are extracted by integrating escaping photons that have direction within $0.1 \leq \cos\theta_i < 0.2$ (or $81.4^\circ \pm 2.9$) and $0.6 \leq \cos\theta_i < 0.7$ (or $49.3^\circ \pm 3.8$). Also, the comparison in the case of $N_{\rm H} = 1 \times 10^{25}$ cm^{-2} and $0.1 \leq \cos\theta_i < 0.2$ are shown. Again, we can see excellent agreement among them in the broadband view while the `MONACO` spectra (green and blue lines) display fluorescent lines of all abundant elements in addition to iron. The `MONACO` spectrum of the bound electron scattering (blue line in the figure) shows higher than the other spectra at the lower energy band below 20 keV. This is also because of the enhancement of Rayleigh scattering, showing consistency with the reduction seen in the direct component.

An interesting difference in the spectral shape appears in the Compton shoulder associated with the iron Kα line, as shown in the right panels of Figure 3. The `MONACO` spectrum of the free electron scattering perfectly agrees with `MYTorus`, simply because the physical conditions assumed in the two models are completely identical. The bound electron case, however, shows a different profile of the Compton shoulder particularly at the low energy edge of the shoulder at 6.24 keV which corresponds to the maximum energy transfer to the recoil electron (i.e. at the scattering angle of 180° with respect to the incident direction). While the case of free electrons at rest shows a sharp edge at 6.24 keV, atomic or molecular binding smears the Compton shoulder profile. This is a result of non-zero momentum of the target electron bound to an atom or molecule which broadens the energy distribution of the scattered photon. This effect by electron binding is quite similar to what we would see if free electrons had thermal motion in a plasma (see e.g. Sunyaev & Churazov,

1998). It is essential to treat scattering by bound electrons for high-resolution spectroscopy to evaluate the Compton shoulder seen in the AGN reflection.

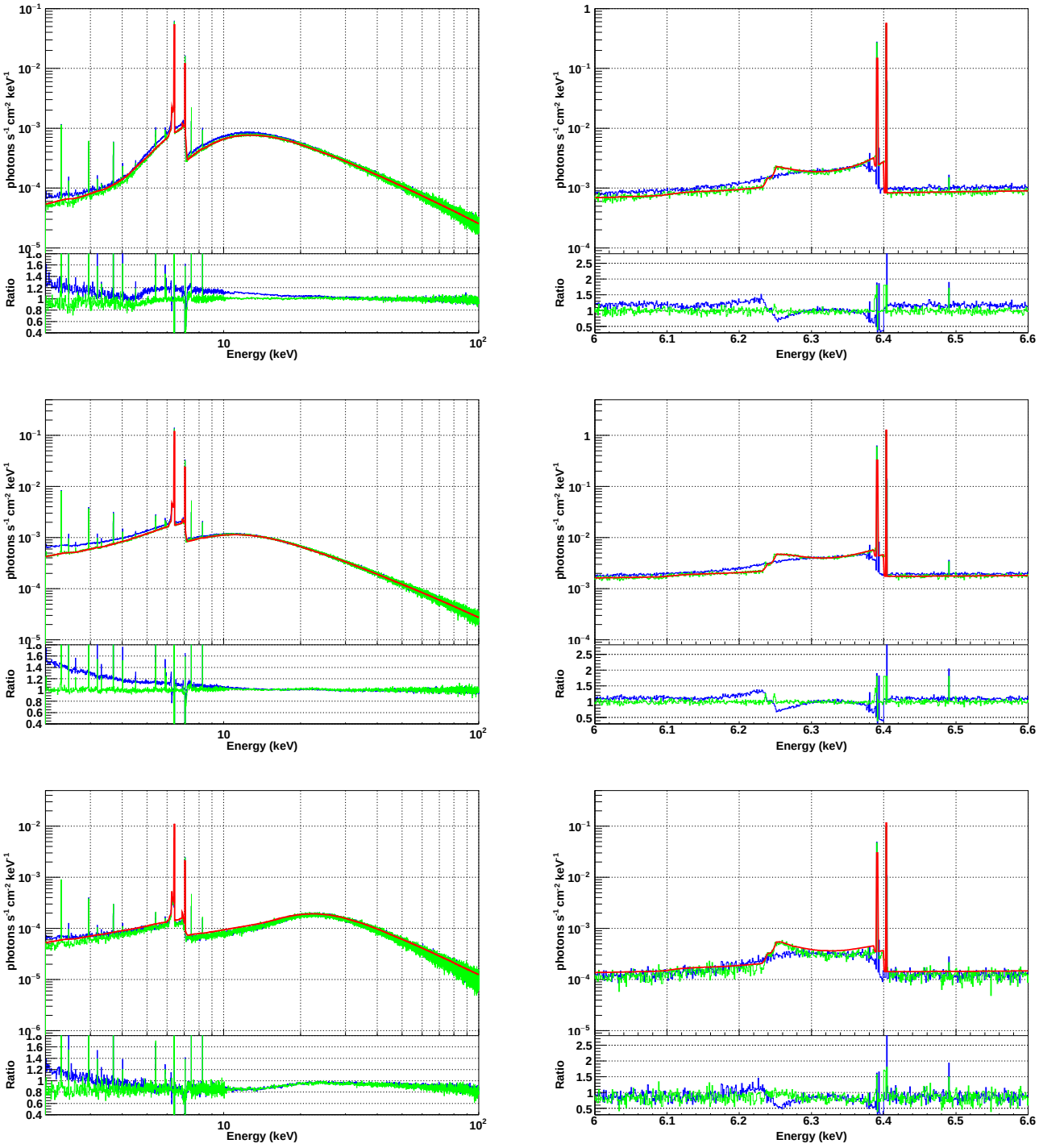

Fig. 3.— Spectra of the reprocessed component for comparison between MONACO and MYTorus. The left panel is shown in 2–100 keV while the right panel is enlarged around the iron Kα line at 6.4 keV. Three models are shown: the MYTorus model (red), the free electron case generated with MONACO (green), and the bound electron case generated with MONACO (blue). (See text in detail). The bottom panels in each figure are spectral ratios against MYTorus. Top and middle are the comparison in the case of $0.1 \leq \cos\theta_i < 0.2$ (or $81.4^\circ \pm 2.9$) and $0.6 \leq \cos\theta_i < 0.7$ (or $49.3^\circ \pm 3.8$) for $N_{\rm H} = 1 \times 10^{24}$ cm^{-2}, respectively, and bottom is in the case of $N_{\rm H} = 1 \times 10^{25}$ cm^{-2} and $0.1 \leq \cos\theta_i < 0.2$.

3. Results

Here, we present X-ray spectra simulated by MONACO for an AGN torus in smooth and clumpy cases, together with behaviors of Comoton shoulder of Fe-Kα line, for various torus conditions. We represent an intrinsic spectrum by a power-law shape with a photon index 1.9 in the range of 2–300 keV, and generated a total number of 10^9 photons for each run. These photons were emitted into any directions within a 4π solid angle from the center isotropically. The abundance are referred to Anders & Grevesse (1989), and hydrogen and helium in the torus are assumed to exist as molecules and atoms, respectively. We sorted the photons going out of the torus into 20 bins evenly spaced in cosine of inclination angles in the range of $-1 \leq \cos\theta_i \leq +1$, where θ_i is the angle between the direction of photon and the z-axis. In this section, if we do not specify torus parameters explicitly, we display X-ray reflection spectra with a condition of $0.1 \leq \cos\theta_i \leq 0.2$ ($\theta_i = 78.46 - 84.26$), $N_{\rm H} = 10^{24}$ cm^{-2}, $\theta_{\rm OA} = 60^\circ$, $A_{\rm metal} = 1.0$ solar, and $V_{turb} = 0$ km s^{-1}. Namely, this fiducial paramter set represents a nearly edge-on view of a torus. We studied the dependences on the column density for both of smooth and clumpy cases, on the inclination and metal abundance for the smooth case, and on the volume filling factor and clump radius for the clumpy case.

Since simulation spectra have poission noise espcially in the high energy band, we created the simulated spectra with 1 eV bin, and then smoothed by running average with 41 bins in $E \leq 8$ keV or $41 + 2\sqrt{(E(\mathrm{keV}) - 8)/0.05}$ bins in $E > 8$ keV, where E is a photon energy. In this case, the smoothing precedure was applied only for the continuum, by excluding the line region. Then, the number of energy bins is 298000.

3.1. Dependence of Hydrogen Column Density (Smooth, Clumpy)

At first, we studied the dependence on the hydrogen column density $N_{\rm H}$ of the torus in the range of $10^{21} - 10^{26}$ cm^{-2}. The simulated spectra of reprocessed component in 2–10 keV are shown in Figure 4. The spectral shape is almost identical to the intrinsic one at low N_H and the flux is almost proportional to N_H; scattering occurs in proportional to N_H, and scattered photons mostly escape out of the torus without absorption in such a Compton-thin regime. Around $N_{\rm H} = 10^{23-24}$ cm^{-2}, the low energy part becomes attenuated and the flux in the high energy part does not increase as N_H becomes larger. At the Compton-thick regime of $N_{\rm H} > 10^{24}$ cm^{-2}, the flux at the high energy part decreases due to the effect of multi scattering. This behavior in the Compton-thick regime is also reported in Ikeda et al. (2009) and Murphy & Yaqoob (2009).

Right panel of Figure 4 shows the spectra around the Fe-K lines. We can see a change of shape and strength of the Compton shoulder against $N_{\rm H}$. The Compton shoulder becomes more apparent for larger $N_{\rm H}$. The Compton shoulder monotonically decreases toward the lower energy at $N_{\rm H} < 10^{24.5}$ cm^{-2}, while a edge-like structure at 6.3 keV becomes prominent at the Compton-thick regime. This behavior can be understood as follows. In figure 19, we summarize the map of locations at which the last interaction between photons and torus for various simulation conditions

and photon energies. Looking at these figures, it is found that, at $N_{\rm H} < 10^{24}$ cm^{-2}, photons in the Compton shoulder come from the whole torus region with a wide range of scattering angle, leading to a wide range of photon energy after Compton scattering. At the Compton-thick regime, most of scattered photons come from the torus behind the central engine with a large scattering angle towards the observer and a large Compton loss, and thus the fraction of photons close to 6.4 keV decreases.

For the clumpy torus, we set a volume filling factor $f = 0.05$ and a clump radius $aR_{\rm torus} = 0.005R_{\rm torus}$. Figure 5 top shows the $N_{\rm H}$-dependence of reflection spectra in the case of the clumpy torus, and figure 5 bottom shows spectral ratios of clumpy to smooth torus. For the viewing angle of $\cos\theta_i = 0.1 - 0.2$, the spectral shape is somewhat different from that of the smooth torus, as seen in the spectral ratio of clumpy to smooth torus. As $N_{\rm H}$ increases, a part of the spectrum becomes humped in the clumpy torus case and the hump moves to the higher energy. From the lower energy part, the flux ratio (for the clumpy torus compared with the smooth case) becomes smaller, and at last the ratio becomes almost constant at ~ 0.6 at $N_{\rm H} = 10^{26}$ cm^{-2} for the clumpy torus than that for the smooth case. As shown in the appendix (figure 20–22), the flux of reprocessed components for the clumpy torus is lower than that for the smooth torus at most inclination angles, except the edge-on ($\cos\theta_i = 0 - 0.1$), in the case of $N_{\rm H} = 10^{26}$ cm^{-2}. This behavior is also reported by Liu & Li (2014); note that the average number of clumps toward the equatorial direction in our case is 7.5 (§2.1). Since the density of each clump is f^{-1} times as high as the average density in the smooth torus case, an effective optical depth is larger and thus the flux becomes lower. The shape of Compton shoulder is also similar but photons close to the line core are somewhat more numerous in the clumpy torus at $N_{\rm H} = 10^{25}$ cm^{-2}, due to that photons scattered at the front of the central engine with a small scattering angle leak to the line of sight easily in the clumpy torus than in the smooth torus around this $N_{\rm H}$.

The dashed line of left panel of Figure 6 shows the equivalent width (EW) of the Fe-Kα line (core plus Compton shoulder); EW is the ratio relative to the sum of reflection and direct continuum. This result is consistent with the previous studies (Ikeda et al. 2009; Murphy & Yaqoob 2009). The dashed line of right panel of Figure 6 shows a integrated flux ratio of the Compton shoulder to the line core. The flux of the Compton shoulder is derived by subtracting the continuum estimated in the wider energy bands adjacent to the line core and the shoulder. The fraction of the Compton shoulder increased with the column density $N_{\rm H}$ in the Compton-thin regime, and saturates at 0.2–0.25 in the Compton-thick regime. This behavior is similar to that in Matt (2002), and reasonably understood as follows. There is a peak at $N_{\rm H} = 10^{24}$ cm^{-2}, the fraction decrease just above the peaking column density is thought to be due to the difference of effective optical depth between line core photons and Compton shoulder photons. The former has one interaction in the torus, while the latter has multiple interactions and thus a large effective optical depth than the former. Therefore, the Compton shoulder becomes prominent faster than the line core at a low $N_{\rm H}$ and its flux decreases faster than the core flux at a high $N_{\rm H}$. Then, the ratio of the Compton shoulder to the line core has a peak between the two regimes.

Solid lines in two panels of figure 6 represent the behavior in the case of the clumpy torus. The dependence of the EW and the fraction of the Compton shoulder against $N_{\rm H}$ is different from those of the smooth torus. The difference of the EW is, however, not so large to distinguish by observations clearly. On the other hand, a fraction of the Compton shoulder is larger by several tens % in the Compton-thick regime for the clumpy torus, compared with the smooth one. This is explained in such a way that the Compton shoulder events which experience multiple interactions could escape from the torus easier in the clumpy torus than in the smooth torus due to intraclump spaces.

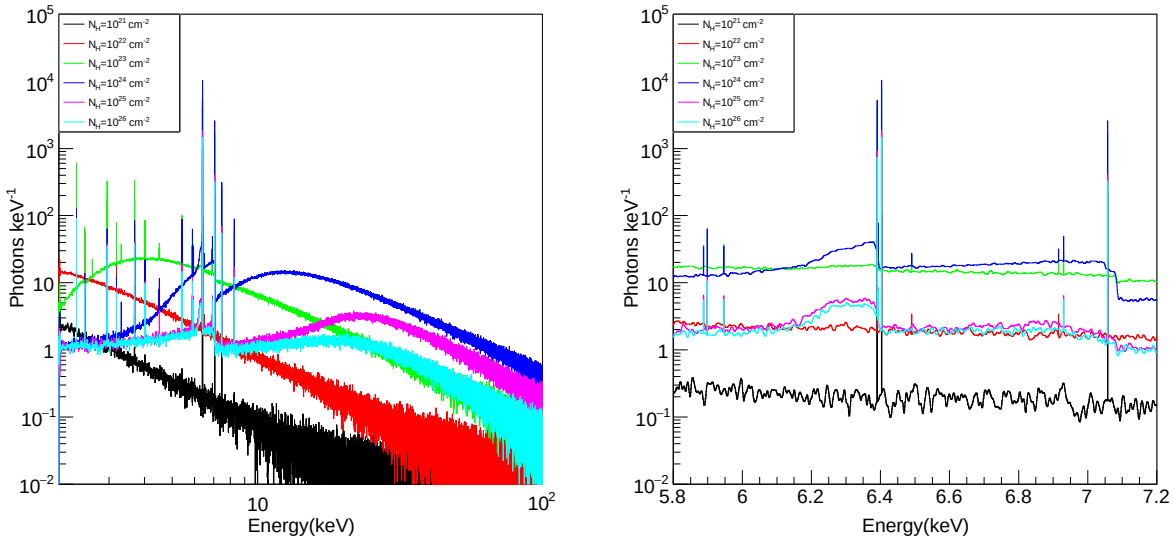

Fig. 4.— Spectra of the reprocessed component in the case of smooth torus with an inclination angle of $\theta_i = 0.1 - 0.2$, for various column densities $N = 10^{21}, 10^{22}, 10^{23}, 10^{24}, 10^{25}$, and 10^{26} cm^{-2}. Right panel is an enlargement around the Fe-K line.

3.2. Dependence of Inclination Angle (Smooth, Clumpy)

Figure 7 shows the simulated reprocessed spectra for $\cos\theta_i$= 0–1 in steps of 0.1 in case of $N_{\rm H} = 10^{24}$ cm^{-2} for the smooth torus. To create this plot, we generate a total number of 10^{10} photons for a run, in order to keep the statistics for arious inclination angles. In the left panel of this figure, the spectral shape and flux are almost identical in high energy band for any inclination angle, since the absorption effect is negligible and scatterings occur with various angles at various positions to reduce the scattering-angle dependence. In the lower energy band, the flux decreases for the larger inclination angle due to the absorption. The shape of Compton shoulder becomes more upward concave at the smaller inclination angle. At $\cos\theta_i = 0.5$–0.9 (θ_i is small), the last scattering position of photons in the Fe-K region includes the equatorial region of the torus behind

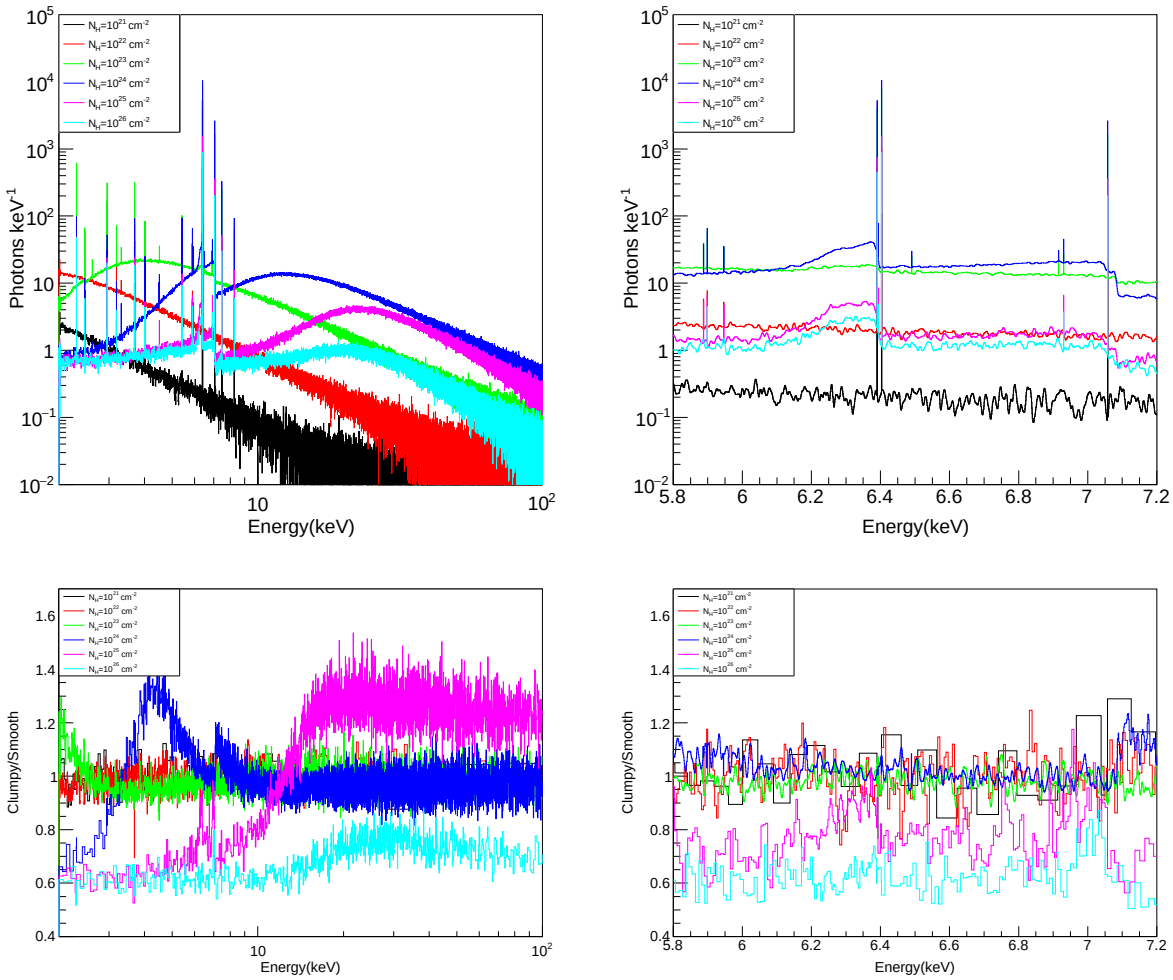

Fig. 5.— (Top) Spectra of the reprocessed component in the case of clumpy torus, for various column densities $N = 10^{21}, 10^{22}, 10^{23}, 10^{24}, 10^{25}$, and 10^{26} cm^{-2}. Right panel is an enlargement around the Fe-K line. (Bottom) Spectral ratios of clumpy to smooth torus for the reprocessed components.

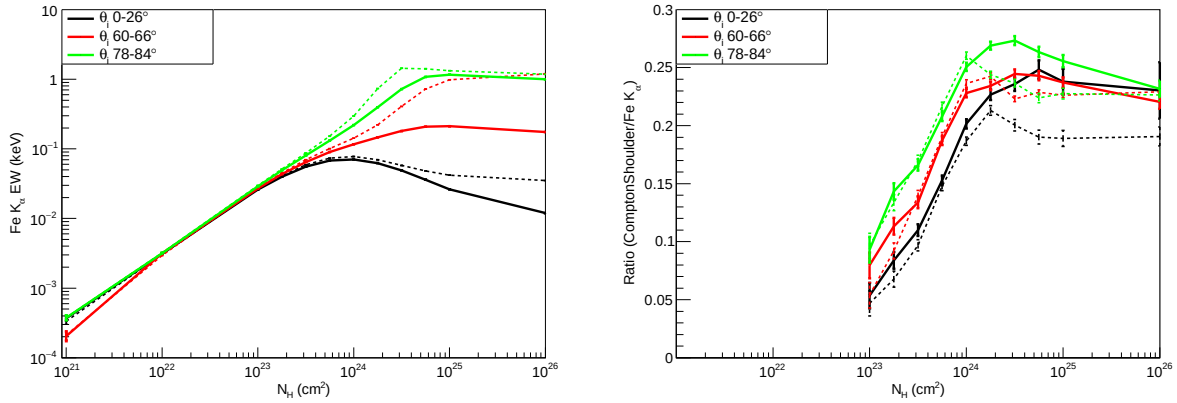

Fig. 6.— Left panel is a Fe-K line (core plus Compton shoulder) equivalent width (EW) against the column density $N_{\rm H}$ for three inclination angles. Right panel is a flux ratio of Fe-K Compton shoulder to line core against $N_{\rm H}$. Solid and dashed lines represent clumpy and smooth torus, respectively.

the central engine from the observer, and the Compton shoulder events scattered in such a region have a large scattering optical depth and thus a lower energy of scattered photons due to Compton loss. At larger inclination angle with $\cos\theta_i < 0.5$, the equatorial region of the torus behind the central engine cannot be observed from the observer, and thus the Compton shoulder events with lower energy decrease.

Figure 8 shows the inclination angle dependence of the Fe-K line EW and the Compton shoulder to the line core ratio for three cases with $N_{\rm H} = 10^{23}$, 10^{24}, and 10^{25} cm^{-2}. This figure shows results for both of smooth and clumpy cases. The inclination angle of the EW jump corresponds to the boundary whether the line from the center to the observer passes the torus or not. This behavior is consistent with that of Murphy & Yaqoob (2009). The fraction of Compton shoulder increases with the inclination angle (i.e., with smaller $\cos\theta_i$ values). For a larger $N_{\rm H}$, the fraction is larger for the clumpy torus than the smooth one, as seen in the $N_{\rm H}$ dependence.

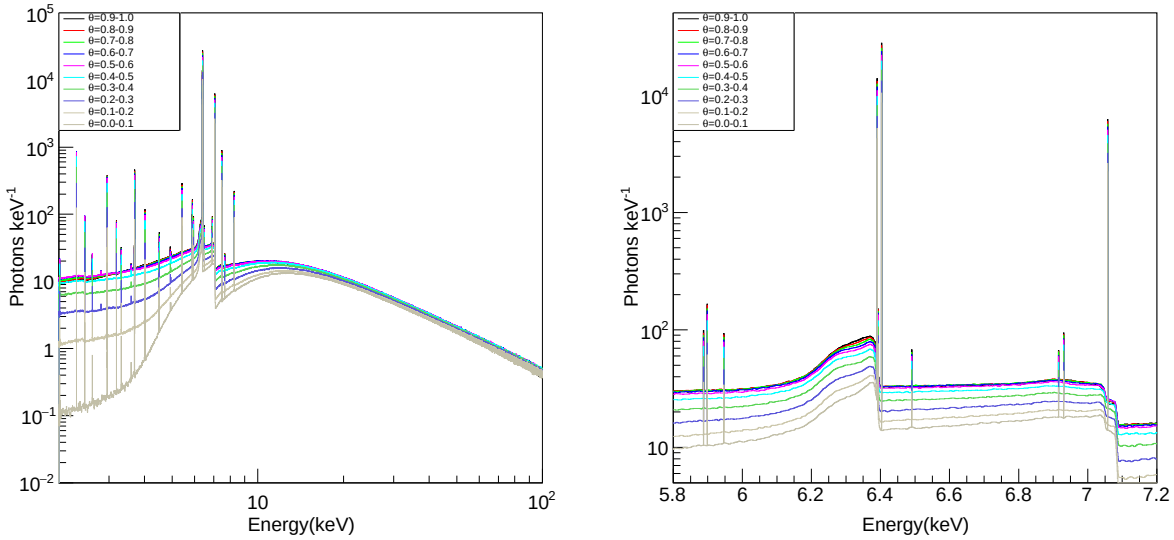

Fig. 7.— Spectra of the reprocessed component in the case of smooth torus with a column density of $N_{\rm H} = 10^{24}$ cm^{-2}, for various inclination angles $\cos\theta_i$ =0.9–1.0, 0.8–0.9, ·, and 0–0.1 from top to bottom. Right panel is an enlargement around the Fe-K line.

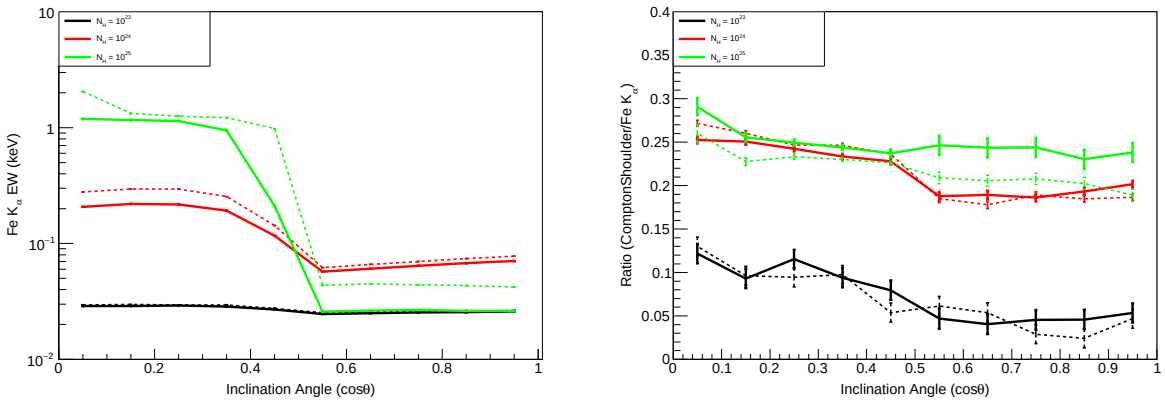

Fig. 8.— Left panel is a Fe-K line (core plus Compton shoulder) equivalent width (EW) against the cosine of inclination angle θ_i for three column densities. Right panel is a flux ratio of Fe-K Compton shoulder to line core against $\cos\theta_i$. Dashed and solid lines correspond to the smooth and clumpy torus, respectively.

3.3. Dependence of Metal Abundance (Smooth, Clumpy)

So far we performed simulation under the condition that metal abundance is the same as the solar system. In this subsection, we studied the dependence on metal abundance. Figure 9 shows the reprocessed spectra on various metal abundances with $N_{\rm H} = 10^{24}$ cm^{-2} for the smooth torus. Metal abundances of heavy elements are kept to follow the solar abundance ratio. For this plot, we generate a total number of 10^{10} photons for $A_{\rm metal} = 3.2$ or 10 in order to keep the statistics, but 10^9 photons for other $A_{\rm metal}$ values. Metal abundance dependence on the reprocessed spectra are similar to that on $N_{\rm H}$, but the difference is that a scattered component in the lower energy part is weak and no flux change in the higher energy band. This is due to that the amount of hydrogen which are main scattering atoms does not change in this case.

Figure 10 and 11 show the EW and the fraction of the Compton shoulder to the line core as a function of metal abundance for three inclination angles. We show two cases of $N_{\rm H} = 10^{24}$ cm^{-2} and 10^{25} cm^{-2} for both of smooth and clumpy cases. At the large inclination angles, EW increases with the metal abundance quasi-proportionally. Looking at the Fe-K line core flux and continuum, this increase is not due to the line flux increase but due to the continuum reduction at high metal abundances. At the small inclination angle, EW does not increase with the metal abundance since the continuum reduction is weak. Interestingly, the fraction of Compton shoulder to the line core is smaller at higher metal abundance. From the spectra in figure 9, the flux of Compton shoulder becomes more heavily reduced than the line core flux at higher metal abundance. At higher metal abundance, the Compton shoulder events which runs a longer path than the line core events in the torus are more strongly absorbed and the flux reduction is large.

For lower metal abundances, the clumpy case gives a higher EW and a lower Compton shoulder to line core ratio than the smooth case. On the other hand, for higher metal abundances, it gives a lower EW. The density in the clumpy case is higher than that in the smooth case with the same $N_{\rm H}$ in our definition. Consider a torus size $R_{\rm torus}$, a clump size $aR_{\rm torus} = 0.005R_{\rm torus}$, and a mean free path $l_{\rm Fe} = 0.035A_{\rm metal}^{-1}R_{\rm torus}$ at the Fe-Kα line energy 6.4 keV under the metal abundance $A_{\rm metal}$ and the volumn filling factor $f = 0.05$. The last one is derived by using the relation between $N_{\rm H}$ and the hydrogen number density $n_{\rm H}$ in section 2.1. In the lower metal abundances, a mean free path $l_{\rm Fe}$ is larger than a clump size $aR_{\rm torus}$ but smaller than a torus size $R_{\rm torus}$. For the clumpy torus, X-rays can efficiently pass through the intraclump space from the central source to the torus, generate the Fe-K lines almost everywhere in each torus, and then efficiently escape out of the torus. In other words, an effective volume to generate Kα line photons is larger for the clumpy torus, and thus EW is larger and Compton shoulder to line core ratio is smaller. For higher metal abundances, $l_{\rm Fe}$ becomes comparable to or smaller than the clump size $aR_{\rm torus}$. In this case, $l_{\rm Fe}$ of the clumpy trus is smaller than that of the smooth torus by a factor of f due to higher density. Since observed Kα line photons come from the region within $l_{\rm Fe}$ of the surface of smooth torus or each clump. As a result, the effective volume to generate Kα line photons is smaller for the clumpy torus, and thus EW is smaller. In addition, the scattering efficiency of Fe-Kα photons also become higher for the clumpy case, the Compton shoulder to line core ratio is similar to that of the smooth torus.

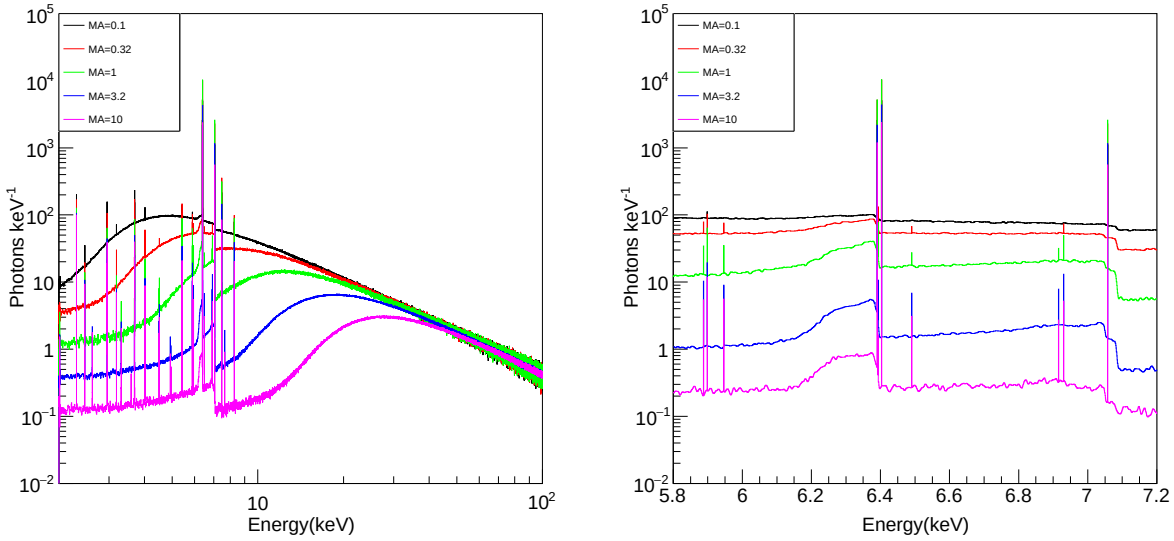

Fig. 9.— Spectra of the reprocessed component in the case of smooth torus with $N_{\rm H} = 10^{24}$ cm^{-2} and $\cos\theta_i = 0.1 - 0.2$, for various metal abundances (MA) in solar unit. Right panel is an enlargement around the Fe-K line.

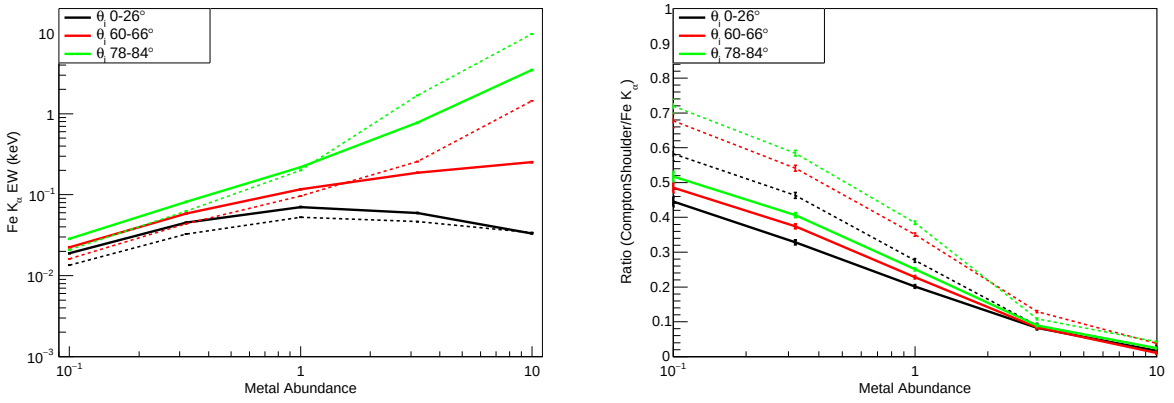

Fig. 10.— Left panel is a Fe-K line (core plus Compton shoulder) equivalent width (EW) against the metal abundance for three inclination angles. Right panel is a flux ratio of Fe-K Compton shoulder to line core against the metal abundance. Both panels are in the case of $N_{\rm H} = 10^{24}$ cm^{-2}. Dashed and solid lines correspond to the smooth and clumpy torus case, respectively.

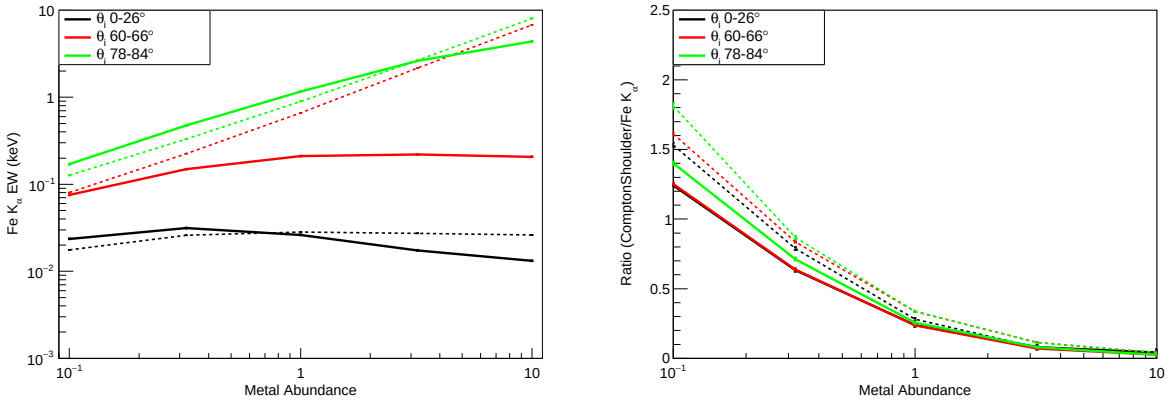

Fig. 11.— Same as figure 10, but in the case of $N_{\rm H} = 10^{25}$ cm^{-2}.

3.4. Dependence of Turbulent Velocity (Smooth, Clumpy)

The matter in the torus might have a Keplarian and random velocity, but here we artificially give a random motion. Figure 12 shows the simulated reprocessed spectra for three $v_{\rm turb}$ for the smooth torus. Fe-K line width is certainly broadened, and the interesting feature is that a part of broadening Kβ line exceeds the absorption edge energy at 7.112 keV (X-ray Transition Energy Database [2]). We can see this fact quantitatively in the Kβ to Kα line ratio in Figure 13. This ratio decreases toward a high random velocity. Of course, this behavior could be dependent on the velocity field. In other words, we can extract the information of the velocity field in the torus from the Kβ to Kα line ratio.

Figure 13 shows that the Kβ to Kα line ratio of the clumpy torus is systematically smaller than that of the smooth one for any velocity dispersion; this difference is due to the difference of torus structure, smooth or clumpy. The difference is more prominent for a small inclination angle. It is found that line intensity ratio of clumpy to smooth torus is smaller for Kβ line than for Kα line. This could be explained as follows. Contrary to the smooth case where line photons escaped from torus can be directly observed, line photons escaped from one clump are absorbed or scattered by front clumps before observed. As a result, the line intensity of the clumpy torus becomes smaller than that of the smooth one. For a smooth torus, observed line photons are generaed mainly at the surface region with a thickness $l_{\rm Fe}$. In this case, Kβ photons can escape more efficiently than Kα photons. On the other hand, for a clumpy torus, generated Kα line photons can escape as efficienctly as Kβ photons, since a clump size $aR_{\rm torus}$ is smaller than a mean free path $l_{\rm Fe}$. Then, the Kβ to Kα line ratio becomes relatively smaller in the clumpy torus.

[2] http://www.nist.gov/physlab/data/xraytrans/index.cfm

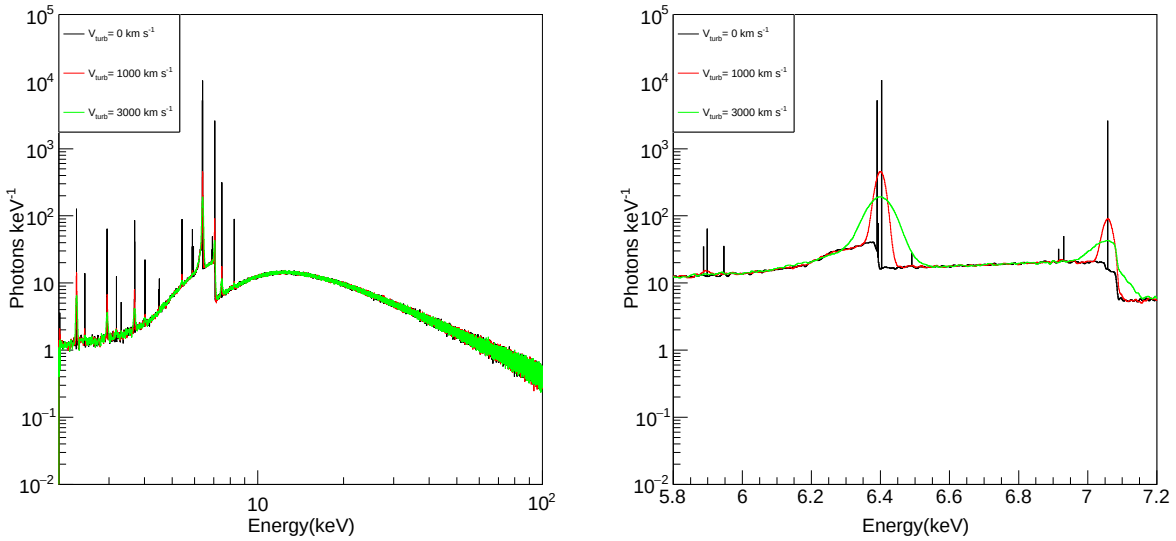

Fig. 12.— Spectra of the reprocessed component in the case of smooth torus with $\cos\theta_i = 0.1 - 0.2$, for various turbulence velocities. Right panel is an enlargement around the Fe-K line.

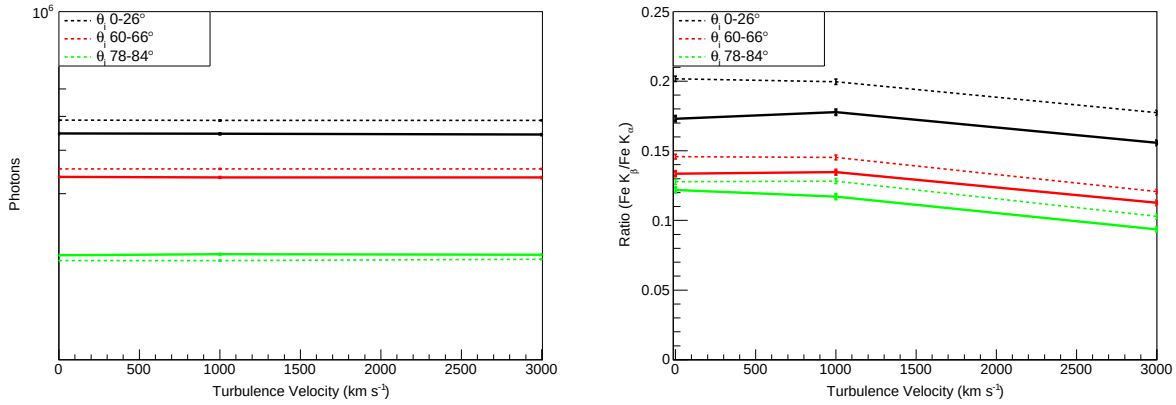

Fig. 13.— Left panel is a Fe-K line (core plus Compton shoulder) equivalent width (EW) against the turbulence velocity for three inclination agn;es. Right panel is a flux ratio of Fe-Kβ to Fe-Kα against the turbulence velocity. Dashed and solid lines correspond to the smooth and torus case, respectively.

3.5. Dependence of volume filling factor and radius of clumps (Clumpy)

We studied the dependence of volume filling factor under the condition that the total $N_{\rm H}$ at the torus mid-plane is fixed to be 10^{24} cm^{-2} and the clump radius is fixed to $aR_{\rm torus} = 0.005R_{\rm torus}$. Accordingly, the number of clump is proportional to the volume filling factor f while the column density of each clump is inversely proportional. Figure 14 shows the reprocessed spectra. We see a difference among spectra in the low and high energy. In the high energy, the flux is smaller for a smaller f, due to a lower scattering efficiency in the torus. On the other hand, in the low energy; the flux is higher for a smaller f since the scattered low-energy photons can easily escape from the torus for a small f. On the other hand, the shape of Compton shoulder is almost identical among different f. We also show the case of the smooth torus for reference, but the shape is almost the same. Quantitatively as shown in figure 15, there is only a weak dependence on f for the EW and the Compton shoulder fraction.

We next varied a clump radius $aR_{\rm torus}$ as $a = 0.005$, 0.003, 0.002 under the condition that the total $N_{\rm H}$ at the torus mid-plane and the volume filling factor f are constant at 10^{24} cm^{-2} and 0.05, respectively. Then, the number of clumps in the torus varies as $\propto a^{-3}$. As shown in figure 16, the reprocessed spectra at higher energy bands are almost identical except for the lowest energy part. As a result, we do not see any dependence on the clump radius for the EW and the fraction of Compton shoulder.

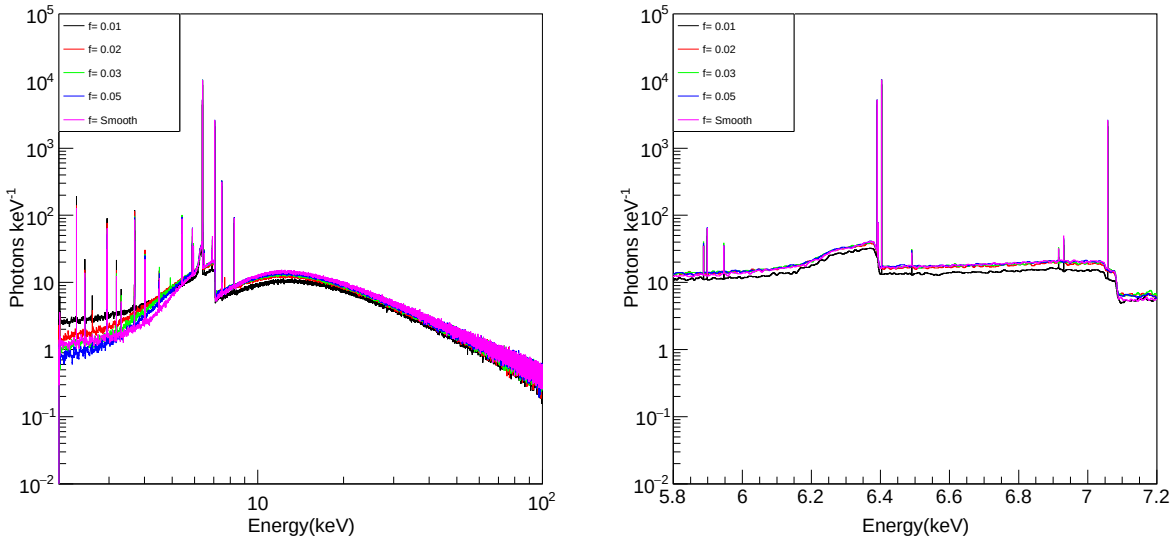

Fig. 14.— Spectra of the reprocessed component in the case of clumpy torus for various volume filling factor f. Right panel is an enlargement around the Fe-K line.

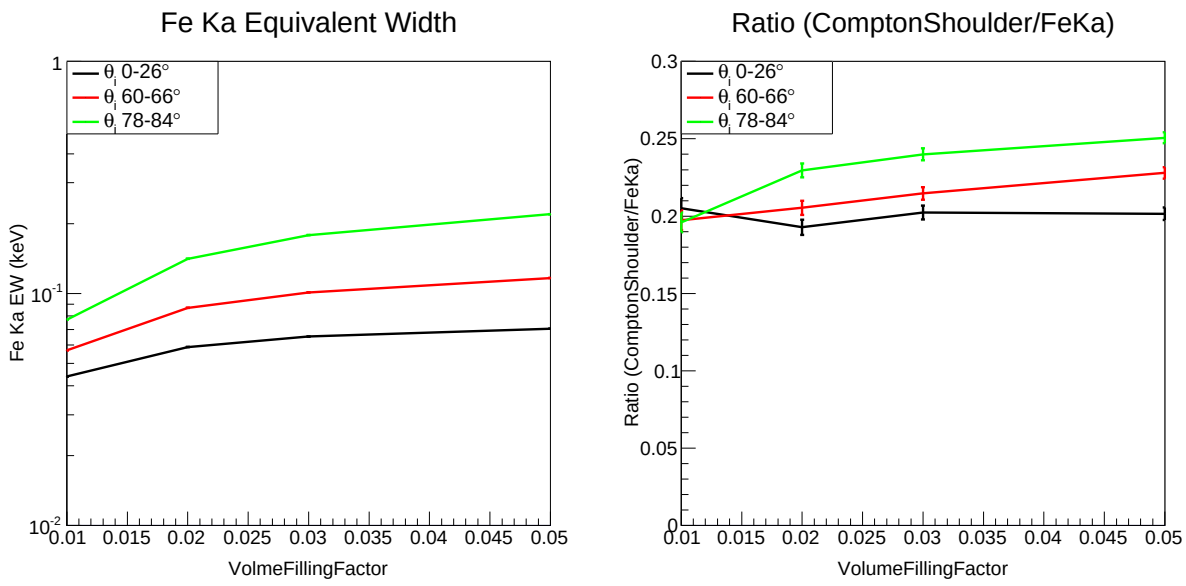

Fig. 15.— Left panel is a Fe-K line (core plus Compton shoulder) equivalent width (EW) against the volume filling factor with $\theta_i = 0.1 - 0.2$. Right panel is a flux ratio of Fe-K Compton shoulder to line core against the volume filling factor for three inclination angles. Both panels are in the case of clumpy torus.

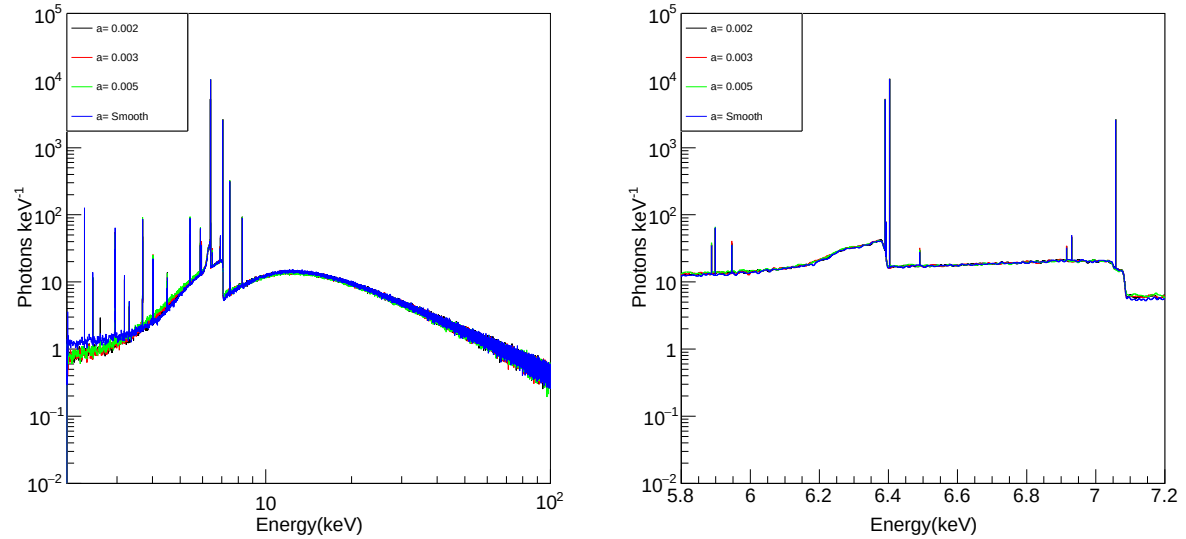

Fig. 16.— Spectra of the reprocessed component in the case of clumpy torus for various clump radii a with $\cos\theta_i = 0.1 - 0.2$. Right panel is an enlargement around the Fe-K line.

4. Discussion

ASTRO-H SXS (Takahashi et al. 2014) will for the first time enable us to perform unprecedentedly fine spectroscopy around the Fe-K line. Compton shoulder and absorption edge structures of the reflection component are interesting and important targets for SXS. Chandra HETG has resolved Compton shoulder clearly for X-ray binaries (Watanabe et al. 2003; Torrejón et al. 2010). On the other hand, Compton shoulder was marginally resolved with HETG for a Seyfert 2 NGC 3783 (Kaspi et al. 2002; Yaqoob et al. 2005) with a very long exposure of 800–900 ks, and for a Seyfert 2 galaxy NGC 4507 with an exposure of 140 ks but with a low significance (Matt et al. 2004). Therefore, SXS will open a new window of Fe-K line spectroscopy with Compton shoulder for AGNs with a normal exposure.

Here we demonstrate simulated spectra of SXS with our constructed X-ray reflection simulator. Models and parameters of simulated spectra are based on the Suzaku observation of a Compton-thick Seyfert 2 galaxy Mrk 3 (Awaki et al. 2008). We model the AGN spectrum with the model `phabs*(powerlaw + zvphabs*powerlaw + reflection)` in the `XSPEC` model. Here, `reflection` is a table model for a clumpy torus, generated by our AGN X-ray reflection simulator. Table 3 summarizes model parameters. In this case, the X-ray flux in 2–10 keV is 8×10^{-12} erg cm^{-2} s^{-1}. We simulated the SXS spectrum with 500 ks exposure, by using SXS response matrices.

Since the advantage of SXS spectroscopic power is to resolve the Compton shoulder with a good signal-to-noise ratio for the first time, we try to constrain torus parameters by spectral fitting only around the Fe-K line. The spectral model is the same as the input model; an absorbed power-law and a smooth torus reflection or a clumpy torus reflection. The parameters of absorption and powerlaw are fixed to the input value, except for a powerlaw normalization (the 6th parameter in table 3). Metal abundance, turbulence velocity, and volume filling factor are also fixed to the input value. That is, free parameters are a powerlaw normalization, torus column density, torus inclination angle, and reflection normalization. We limited the energy band to 6.0–6.7 keV, and obtained the confidence contour.

Figure 17 shows a simulated SXS spectrum around the Fe-K line. Compton shoulder is clearly resolved, and also Kα_1 and Kα_2 are separated, demonstrating the SXS power. Figure 18 shows confidence contours between column density and inclination angle for fitting with smooth or clumpy torus. These figures demonstrate that spectral fitting only around Fe-Kα line can constrain reflection parameters by using the Compton shoulder, and thus gives us a new tool to study the torus structure. Thus, together with the broad-band spectral fitting of continuum, better constraint could be available. The behavior of contours are different between smooth and clumpy models. This is due to the different dependence on the column density for the Compton shoulder to core intensity ratio between two models as shown in figure 6 right.

Therefore, this demonstrates that the correct modeling of the Compton shoulder is very important to probe the torus condition by using the Compton shoulder. In terms of this view point, our model considers the different shape of Compton shoulder between bound and free electrons and

also that between atoms and molecules.

Table 3: Model parameters for *ASTRO-H* SXS simulation for the `XSPEC` model: `phabs*(powerlaw + zvphabs*powerlaw + reflection)`

component	parameter	unit	value
zvphabs	$N_{\rm H}$	10^{22} cm^{-2}	8.7×10^{-2}
powerlaw	Index		1.8
powerlaw	norm^a		1.27×10^{-4}
phabs	$N_{\rm H}$	10^{22} cm^{-2}	110
powerlaw	Index		1.8
powerlaw	norm^a		5×10^{-3}
Reflection	$N_{\rm H}$	10^{22} cm^{-2}	3×10^2
Reflection	Inclination $\cos\theta_i$		0.5
Reflection	Metal Abundance	solar	1.0
Reflection	Turbulence Velocity	km s^{-1}	0
Reflection	Volume Filling Factor		0.005

a: Normalization in unit of photons cm^{-2} s^{-1} keV^{-2} @ 1 keV.

The `MONACO` frame work on which our model is constructed has more advantages to explore the torus model furthermore. For example, X-ray reflection spectral modeling by ionized material and velocity structure of torus material can be implemented, as constructed for simulation of AGN outflow (Hagino et al. 2015). Time history of reflection spectra after flares of the central engine can be also tracked, as applied for the Galactic center (Odaka et al. 2011). In contrast with a smooth torus model, a clumpy torus likely exhibits a fluctuation of spectral shape for different azimuthal angles even with the same inclination angle. In a forthcoming paper, we will investigate to what extent such variations will appear. In this paper, we construct a simple torus geometry, but more complex structure of torus that has been recently suggested can be modeled. If the UV from the central accretion disk controls the innermost edge of a dusty tori, the shape of the inner part of the torus must be significantly different from that of the donut-like tori. Namely, a strong anisotropy of the disk (Netzer 1987) makes the innermost edge of the torus concave (Kawaguchi & Mori 2010; 2011). At low latitudes of the torus (close to the midplane of the disk), the dusty torus exists very close to the outermost edge of the accretion disk. This region, where the rotational and turbulent velocity are likely large (some thousands km s^{-1}; Kawaguchi 2013), may affect the line profile of emission lines (e.g., core to wing ratio), time response of the line flux and profile, and the viewing angle dependence of the Fe-K lines. In a future paper, we will examine how the innerpart structure of the torus changes the overall results.

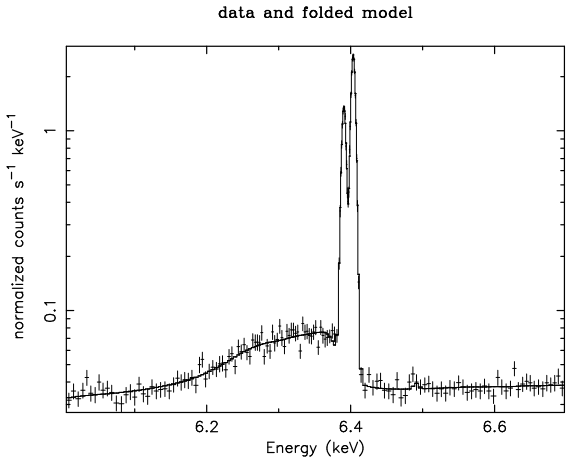

Fig. 17.— Simulated *ASTRO-H* SXS spectra for Mrk 3 around the Fe-K line (6.0–6.7 keV), based on our clumpy torus model. Solid line represents the best-fit model. See the detail in the text.

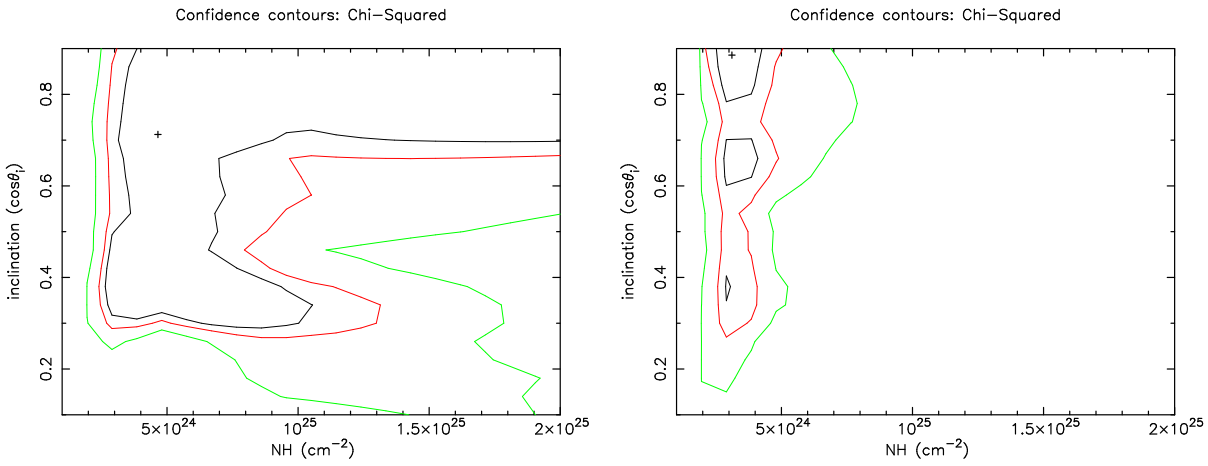

Fig. 18.— Confidence contours between column density and inclination angle for spectral fitting of the simulated *ASTRO-H* SXS spectrum only around the Fe-K line. Black, red, and green lines represent 68%, 90% and 99% confidence levels, respectively. See the detail in the text. Left and right are for the smooth and clumpy cases, respectively. "+" reoresents a location of the best-fit values.

5. Conclusions

We construct an X-ray spectral model of a torus in AGN with a Monte Carlo simulation framework `MONACO`. Two torus geometries of smooth and clumpy cases are considered. In order to reproduce a Compton shoulder accurately, `MONACO` includes not only free electron scattering but also bound electron scattering. Raman and Reyleigh scattering are also treated, and scattering cross sections dependent on chemical states of hydrogen and helium are included. Doppler broadening by turbulence velocity can be implemented. We compared our simulation spectra with a widely used X-ray spectral model `MYTorus`, and found almost consistent results. We studied the dependence of reprocessed X-ray spectra, especially for Fe-K line Compton shoulder on various torus parameters, such as Hydrogen column density along a line on the equitorial plane, inclination angle from the line of sight, metal abundance, turbulence velocity for both smooth and clumpy cases, volumn filling factor and clump scale radius for the clumpy case. The fraction and shape of Compton shoulder depends on the column density, and the dependence is different between smooth and clumpy cases. Also, a weak dependence of Compton shoulder shape on the inclination angle is seen. An equivalent width of Fe-K core and Compton shoulder and a fraction of Compton shoulder largely depend on the metal abundance. Only a weak dependence of Compton shoulder fraction is seen for turbulence velocity, filling factor, and clump scale radius. We found that a intensity ratio of Compton shoulder to line core mainly depends on the column density, inclination angle, and metal abundance. For instance, an increase of metal abundance makes the Compton shoulder relatively weak. Also, shape of Compton shoulder depends on the column density. Then, we present the *ASTRO-H* SXS simulated spectra of Mrk 3 and found to a clear Compton shoulder in the spectrum. Even with a narrow-band spectral fitting only around the Compton shoulder, we will be able to put some constraints on the torus geometry.

Position maps of last scattering of Compton shoulder photons

Please see the original journal for figure 19, since the file size exceeds the astro-ph limit.

Fig. 19.— Position maps of last scattering of Compton shoulder photons in 6–6.39 keV for various column densities $N_{\rm H}$. The observer locates toward the inclination angle of $\cos\theta_i = 0.1 - 0.2$ in the X-Z plane. Left panle is a map in the X-Y plane, where the observer is located towards the right direction. Middle-left, middle-right, are right are maps within the torus integrated over the 1st quadrant ($y > -x$ and $y < x$; i.e., close to the observer), 2nd quadrant ($y > -x$ and $y > x$), and 3rd quadrant ($y < -x$ and $y > x$; i.e., behind the central engine with respect to the observer), respectively.

Comparison of Reprocessed Spectra between Clumpy and Smooth Torus

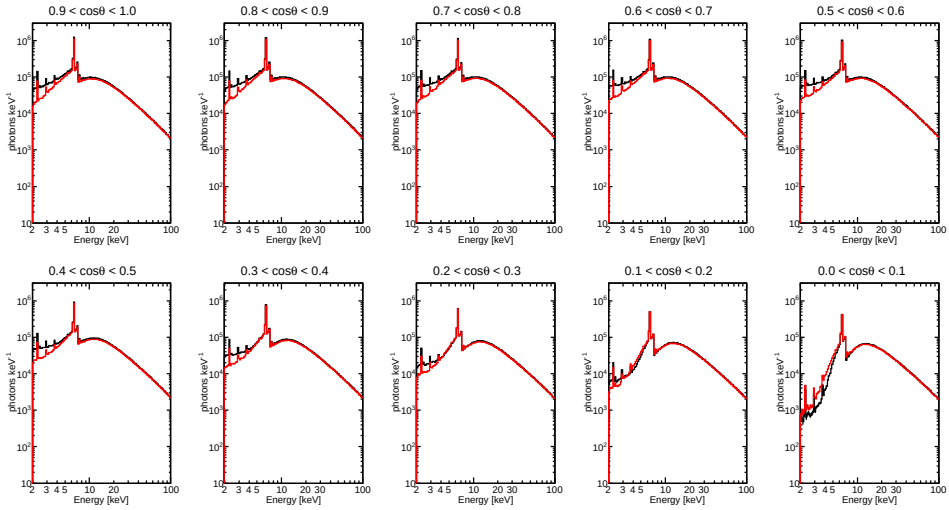

Fig. 20.— Comparison of Reprocessed Spectra between Clumpy and Smooth Torus for various inclination angles of $\cos\theta_i = 0 - 1$ with a step of 0.1 in the case of $N_{\rm H} = 10^{24}$ cm^{-2}. Black and red spectra correspond to smooth and clumpy torus, respectively.

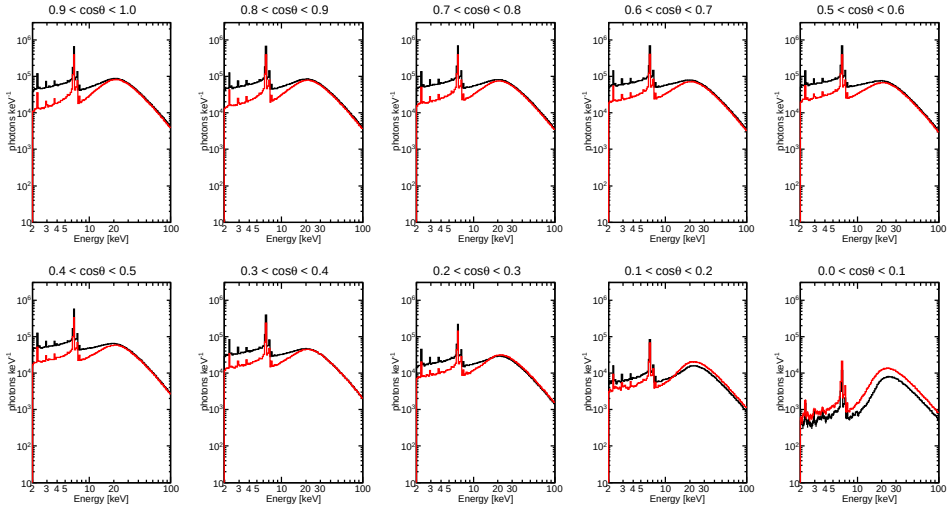

Fig. 21.— Same as figure 20 but in the case of $N_{\rm H} = 10^{25}$ cm^{-2}.

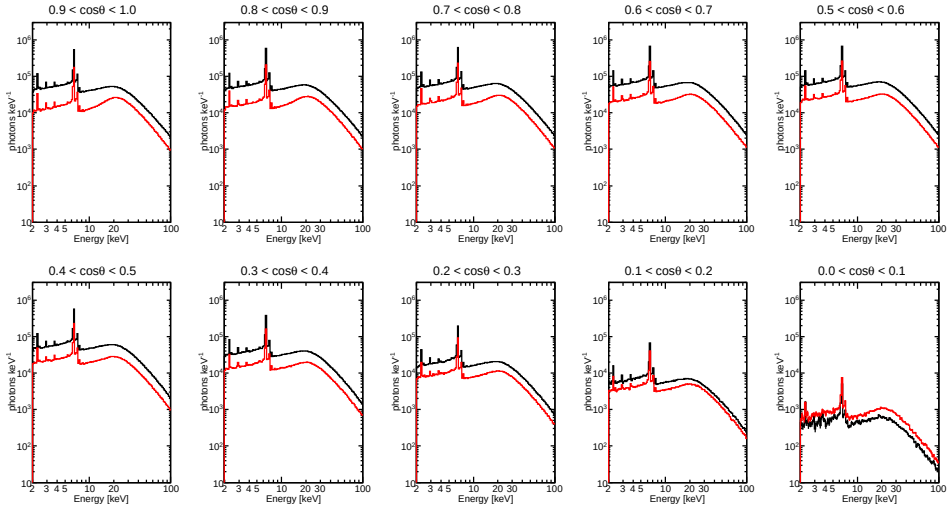

Fig. 22.— Same as figure 20 but in the case of $N_{\rm H} = 10^{26}$ cm^{-2}.

REFERENCES

Agostinelli, S., Allison, J., Amako, K., et al. NIM-A, 506, 250

Allison, J., Amako, K., Apostolakis, J., et al. 2006, IEEE Trans. Nucl. Sci. 53, 270

Anders, E., & Grevesse, N. 1989, Geochim. Cosmochim. Acta, 53, 197

Antonucci, R. R. J., & Miller, J. S. 1985, ApJ, 297, 621

Awaki, H., Koyama, K., Inoue, H., & Halpern, J. P. 1991, PASJ, 43, 195

Awaki, H., Anabuki, N., Fukazawa, Y., et al. 2008, PASJ, 60, 293

Barvainis, R. 1987, ApJ, 320, 537

Brightman, M., & Nandra, K. 2011, MNRAS, 413, 1206

Brightman, M., Baloković, M., Stern, D., et al. 2015, ApJ, 805, 41

Ertuğral, B., Apaydın, G., Çevik, U., Ertuğrul, M., & Kobya, A. İ. 2007, Radiation Physics and Chemistry, 76, 15

Fukazawa, Y., Hiragi, K., Mizuno, M., et al. 2011, ApJ, 727, 19

Hagino, K., Odaka, H., Done, C., et al. 2015, MNRAS, 446, 663

Hönig, S. F., Beckert, T., Ohnaka, K., & Weigelt, G. 2006, A&A, 452, 459

Ikeda, S., Awaki, H., & Terashima, Y. 2009, ApJ, 692, 608

Ivanchenko, Y. N., and Geant4 Collaboration, 2003, NIM-A 502, 666.

Kaspi, S., Brandt, W. N., George, I. M., et al. 2002, ApJ, 574, 643

Kawaguchi, T., & Mori, M. 2010, ApJ, 724, L183

Kawaguchi, T., & Mori, M. 2011, ApJ, 737, 105

Kawaguchi, T. 2013, arXiv:1306.0188

Krause, M. O. 1979, Journal of Physical and Chemical Reference Data, 8, 307

Krolik, J. H., & Begelman, M. C. 1988, ApJ, 329, 702

Krolik, J. H., & Lepp, S. 1989, ApJ, 347, 179

Laor, A., & Draine, B. T. 1993, ApJ, 402, 441

Liu, Y., & Li, X. 2014, ApJ, 787, 52

Liu, Y., & Li, X. 2015, MNRAS, 448, L53

Magdziarz, P., & Zdziarski, A. A. 1995, MNRAS, 273, 837

Matt, G. 2002, MNRAS, 337, 147

Matt, G., Bianchi, S., D'Ammando, F., & Martocchia, A. 2004, A&A, 421, 473

Murphy, K. D., & Yaqoob, T. 2009, MNRAS, 397, 1549

Nandra, K., O'Neill, P. M., George, I. M., & Reeves, J. N. 2007, MNRAS, 382, 194

Nenkova, M., Sirocky, M. M., Nikutta, R., Ivezić, Ž., & Elitzur, M. 2008, ApJ, 685, 160

Netzer, H. 1987, MNRAS, 225, 55

Odaka, H., Aharonian, F., Watanabe, S., et al. 2011, ApJ, 740, 103

Pier, E. A., & Voit, G. M. 1995, ApJ, 450, 628

Sunyaev, R. A., & Churazov, E. M. 1996, Astronomy Letters, 22, 648

Sunyaev, R., & Churazov, E. 1998, MNRAS, 297, 1279

Takahashi, T., Mitsuda, K., Kelley, R., et al. 2014, Proc. SPIE, 9144, 914425

Thompson, A. C., et al. 2001, X-ray Data Booklet (Berkeley, CA: Lawrence Berkeley National Laboratory)

Torrejón, J. M., Schulz, N. S., Nowak, M. A., & Kallman, T. R. 2010, ApJ, 715, 947

Watanabe, S., Sako, M., Ishida, M., et al. 2003, ApJ, 597, L37

Yaqoob, T., Reeves, J. N., Markowitz, A., Serlemitsos, P. J., & Padmanabhan, U. 2005, ApJ, 627, 156

Yaqoob, T., & Murphy, K. D. 2011, MNRAS, 412, 277

This preprint was prepared with the AAS LaTeX macros v5.2.